Slip rate estimation along the western segment of the Main Marmara Fault over the last 405–490 ka by correlating mass transport deposits

C. Grall,[1,2] P. Henry,[1] Y. Thomas,[2] G. K. Westbrook,[2] M. N. Çağatay,[3] B. Marsset,[2] H. Saritas,[4] G. Çifçi,[4] and L. Géli[2]

[1]   High-resolution 3-D seismic data acquired in the Sea of Marmara on the Western High, along the northwestern branch of the North Anatolian Fault (also known as the Main Marmara Fault), shed new light on the evolution of the deformation over the last 500–600 ka. Sedimentary sequences in ponded basins are correlated with glacioeustatic cycles and transitions between marine and low sea/lake environments in the Sea of Marmara. In the 3×11 km^2 of the 3-D seismic survey, deformation over the last 405–490 ka is localized along the main fault branch and north of it, where N130°–N140° trending normal faults and N40°–N50° folding accommodated strike-slip deformation associated with active argillokinesis. There is some evidence that deformation was more distributed further back in the past, at least over the depth range (<600 m below seafloor) of our survey. A N110° basin and buried ridge system were eventually cut by the presently active fault. The southern part of the basin was then uplifted, while the northern part was folded but continued to subside along the fault. A mass transport deposits complex dated between 405–490 ka shows a lateral displacement of 7.7 ± 0.3 km, corresponding to an estimated slip rate of 15.1–19.7 mm/a. We conclude that this strand of the Main Marmara Fault on the Western High has taken up most of the strike slip motion between the Anatolian and Eurasian plates over the last 405 ka at least.

1.   Introduction

[2]   The Sea of Marmara is a strike-slip basin along the North Anatolian Fault (NAF) that has been intensively studied in great part because of the threat of large earthquakes and tsunamis that offshore active faults present for the Istanbul area. Although the Sea of Marmara is one of the best known examples of a pull-apart basin, there remain unsolved issues regarding segmentation, fault slip rate, and tectonic evolution that have general implications for the understanding of continental strike-slip system and related geohazards. The NAF is a dextral transform continental fault, which accommodates the motion of the Anatolian plate relative to the Eurasian

plate, determined by GPS to about 20–27 mm/yr (Figure 1a) [*Meade et al.*, 2002; *Le Pichon et al.*, 2003; *Reilinger et al.*, 2006; *Hergert and Heidbach*, 2010; *Le Pichon and Kreemer*, 2010]. At the eastern end of the Sea of Marmara, the NAF splits into two main branches (Figure 1b) [*Şengör et al.*, 2005; *Flerit et al.*, 2003]. The northern branch takes up most of the strike-slip motion and runs through the Sea of Marmara. GPS data show the total displacement rate across this part of the fault system in the Sea of Marmara to be 18 ± 2 mm/yr [*Reilinger et al.*, 2010], with an oblique component that can account for the subsidence of the deep basins and crustal thinning [*Bécel et al.*, 2009]. The geometry of active faults in the Sea of Marmara has been defined from high-resolution bathymetry, subbottom profiles, and seismic data acquired at various scales [*Le Pichon et al.*, 2001; *Imren et al.*, 2001; *Parke et al.*, 2002; *Armijo et al.*, 2002; *Carton et al.*, 2007; *Bécel et al.*, 2010].

[3]   A continuous fault system, the Main Marmara Fault (MMF), connects the Izmit and the Ganos faults across the Sea of Marmara [*Le Pichon et al.*, 2003] (Figure 1b). This fault may be divided in two or three segments (Figure 1b), the Western, the Istanbul, and the Çınarcık segments, that could rupture independently during large earthquakes [*Parsons*, 2004; *Pondard et al.*, 2007; *Oglesby et al.*, 2008]. Several active fault branches splay from the MMF [*Armijo et al.*, 2002] and may represent flower structures rooting in a single

Additional supporting information may be found in the online version of this article.

[1]CEREGE, CNRS, Aix Marseille University, Marseille, France.
[2]IFREMER - French Research Institute for Exploration of the Sea, Marine Geosciences, Plouzané, France.
[3]Istanbul Technical University, EMCOL and Department of Geological Engineering, Istanbul, Turkey.
[4]Institute of Marine Sciences and Technology, Marine Geophysics, Izmir, Turkey.

Corresponding author: C. Grall, CEREGE, CNRS, Aix Marseille University, 3 place Victor Hugo, case 67, FR-13331, Marseille, France. (grall@cerege.fr)
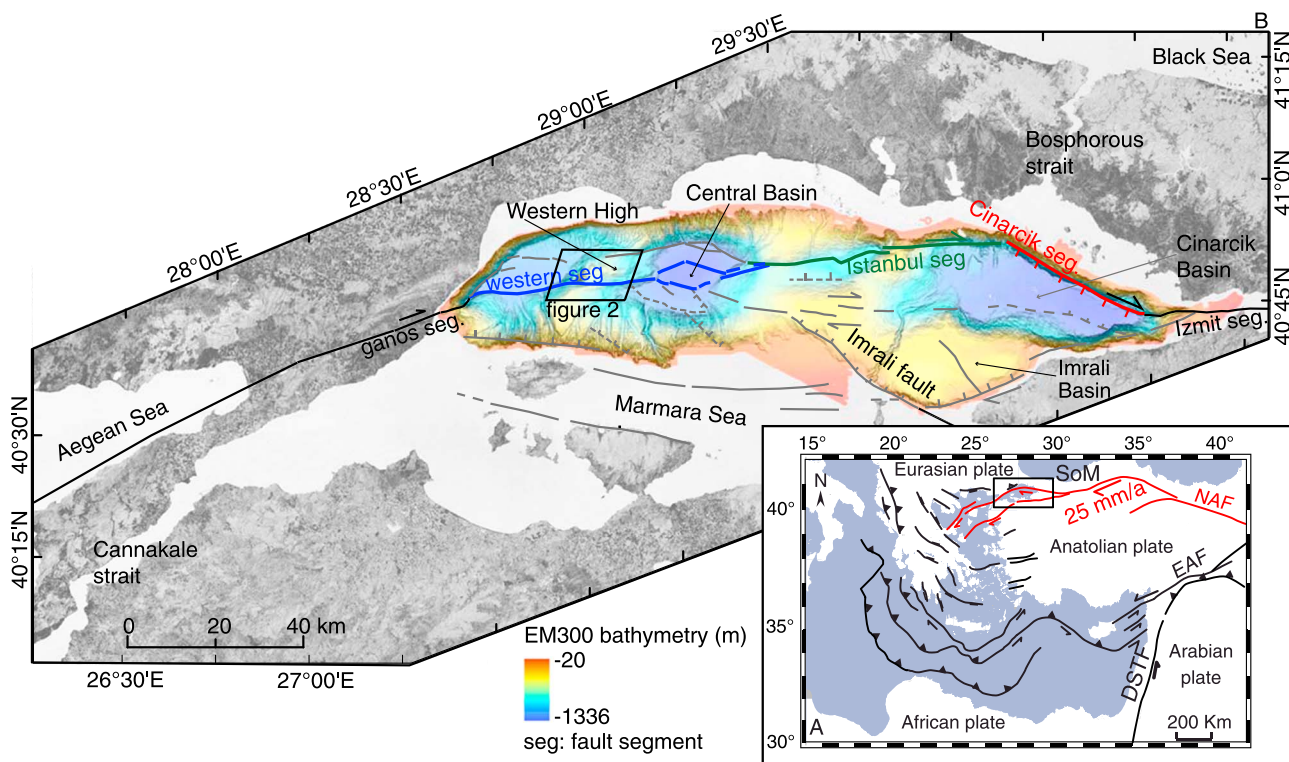
Figure 1. (a) Tectonic setting of the Eastern Mediterranean is shown. Lines indicate active faults and major plate boundaries. The abbreviations are NAF (North Anatolian Fault), EAF (East Anatolian Fault), and DSTF (Dead Sea Transform Fault). The mean motion between Anatolian and Eurasian plates [*Meade et al.*, 2002; *Le Pichon et al.*, 2003; *Reilinger et al.*, 2006; *Hergert and Heidbach*, 2011; *Le Pichon and Kreemer*, 2010] is also mentioned. Inset shows the location of the Sea of Marmara (SOM). (b) Bathymetric map of the Marmara Trough with the main structures [*Grall et al.*, 2012] is shown. The Main Marmara Fault is shown by thick lines and comprises the Western (in blue), the Istanbul (in green), and the Cinarcik (in red) segments. The MMF linked the Ganos and the Izmit segments [*Le Pichon et al.*, 2003]. Faults in grey are the secondary fault systems [*Parke et al.*, 1999]. The black inset locates Figure 2.

crustal or lithospheric shear zone [*Bécel et al.*, 2009, 2010]. Mechanical models constrained by GPS data suggest that, because of these complexities, the strike-slip rate along the MMF may vary between fault segments, ranging between 12 and 18 mm/yr, constituting half to two thirds of the total Eurasia-Anatolia motion [*Hergert and Heidbach*, 2010]. However, the strike-slip velocity on off-shore faults in the Sea of Marmara remains largely unconstrained. On land, stream terraces and alluvial fans are often used as markers to measure the long-term lateral offsets of fault zones. In central North Turkey where the NAF is a single fault, fluvial terrace correlations suggest that the Holocene slip rate is consistent with the slip rate deduced from the GPS data in this region [*Hubert-Ferrari et al.*, 2002]. In the eastern part of the Sea of Marmara, offset of shallow water geomorphology during the Holocene yielded slip rates for the Izmit and Gemlik faults (Figure 1) that imply partitioning of strike-slip motion between the Izmit and Gemlik faults [*Polonia et al.*, 2004; *Gasperini et al.*, 2011]. In the western part of the Sea of Marmara, however, the MMF may take a larger fraction of the strike-slip motion. For instance, mechanical modeling based on GPS data that suggests slip on the Western High segment may account for nearly all of the 18 ± 2 mm/yr motion across the Sea of Marmara, consistent with

paleoseismological slip estimates on Ganos Fault, e.g., [*Hergert and Heidbach*, 2010; *Reilinger et al.*, 2010].

[4] Another debated issue is the evolution with time of fault-network geometry and kinematics since the initiation of the NAF system in the Sea of Marmara, which is thought to have occurred 5 Ma ago at the earliest [*Şengör et al.*, 2005; *Armijo et al.*, 1999]. Steady state models for crustal thinning and subsidence have been proposed, based on pull-part fault geometry and shear partitioning [*Armijo et al.*, 2002] or on oblique slip on nonvertical through-going master faults [*Seeber et al.*, 2004; *Okay et al.*, 2000, 2004]. On the other hand, it was also proposed that the MMF could be a recent structure about 200 ± 100 ka old, crosscutting an older system of pull-apart basins [*Le Pichon et al.*, 2003; *Rangin et al.*, 2004]. Studies of deep basin structure show evidence for changes in the subsidence pattern with time [*Carton et al.*, 2007; *Bécel et al.*, 2010; *Grall et al.*, 2012], but these changes are gradual as the present day subsidence pattern may have remained in steady state for several hundred thousand years, at least 500 ka for the Imrali and Kumburgaz basin [*Sorlien et al.*, 2012], and about 330 ka in the Central Basin [*Grall et al.*, 2012]. Current understanding of the tectonic evolution in the Sea of Marmara relies primarily on observations in the basins that constrain the vertical component of motion on faults. Independent estimates on horizontal
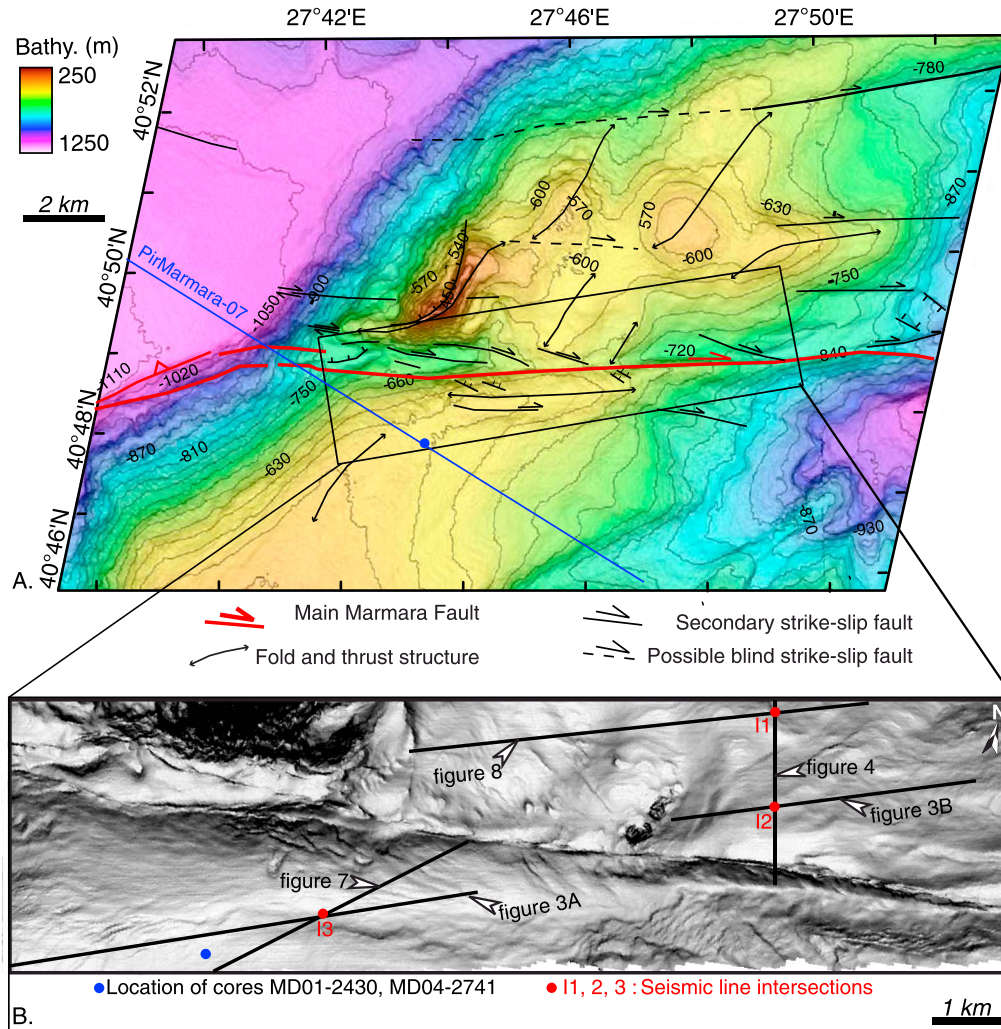
Figure 2. (a) Bathymetric map of the Western High with the main structures is identified on the bathymetry. The Main Marmara Fault is shown by thick red lines. The Western High is formed by N45° trending folds and thrusts [*Imren et al.*, 2001; *Rangin et al.*, 2004] presumably offset by some secondary strike-slip faults. The surface traces of some secondary strike-slip faults can be followed on the bathymetry (in solid black lines); others are supposed regarding the offset of folds and thrusts structures (in dashed black lines). The black inset located the 3-D seismic volume that is located within the 3 km wide swath along MMF. N105° faults connected to the MMF within the fault zone are indicated. Please refer to the Figure 6 for more details about these faults. Stacking velocities have been carried out along the 2-D long-offset PriMarmara-07 seismic line shown by the blue line. The cores MD01-2430 and MD04-2741 which provided a high-resolution age model over the last ~29 ka [*Vidal et al.*, 2010, and this study] are located by a blue circle. (b) High-resolution slope gradient map derived from the seafloor peaking over the 3-D seismic data. The 3-D high-resolution survey was carried out using two streamers (of 48 traces) and two high-frequency air gun sources (45–175 Hz at −6dB). Lateral resolution is estimated between 13 and 25 m on the migrated seismic volume (bin size 6 m) at the seabed, and the vertical resolution is of 3.5 m [*Thomas et al.*, 2012]. Black lines correspond to track lines of seismic reflection profiles shown in the paper, and the red circle indicated the intersection between profiles mentioned in Figure 3, 4, 7, and 8. The black circle indicated the location of the cores used in this study.

slip velocities are generally lacking. It thus appears important to gain better knowledge of the ages of the active fault strands crossing the highs and of their horizontal slip rates.

[5] The objective of the work reported in this paper is to estimate the slip rate and to characterize the deformation along the MMF in the Western High, where high-resolution 3-D seismic data [*Thomas et al.*, 2012] (Figure 2a) were acquired. The 3-D high-resolution survey covers an 11 by 3.3 km² area

of the western part of the Western High, straddling the main strike-slip fault branch of the MMF (Figure 2a). The Western High 3-D seismic data set displays several complexes of mass transport deposits (MTDs) in ponded basins, including one apparently offset by the main strike-slip fault, used to determine the horizontal component of slip. The age of the MTDs is estimated from their positions within the stratigraphic sequences, which we correlated with global eustatic

cycles. Such correlations have been previously performed throughout the eastern part of the Sea of Marmara [*Sorlien et al.*, 2012; *Seeber et al.*, 2006] and in the Central Basin [*Grall et al.*, 2012]. We extend these correlations to the Western High. The approach is explained in more detail in section 2.

2. Methods and Stratigraphic Model Construction

2.1. Stratigraphic Sequences in the Sea of Marmara: Background

[6] Glacioeustatic cycles determine the periods of connection between the Marmara, the Mediterranean, and the Black seas across the Dardanelles and Bosphorous sills [*Ryan et al.*, 1997; *Aksu et al.*, 1999; *Mudie et al.*, 2002; *Kaminski et al.*, 2002; *Vidal et al.*, 2010; *Çağatay et al.*, 2000, 2003, 2009; *Badertscher et al.*, 2011]. The Sea of Marmara has thus undergone transitions between a salty marine environment, when connected to the Mediterranean Sea, and a brackish environment, frequently influenced by outflow from the Black Sea, depending on the global sea level, the climatic conditions, and the depth of the Dardanelles sill [*Çağatay et al.*, 2009; *Vidal et al.*, 2010]. Considering global sea level variations [e.g., *Lisiecki and Raymo*, 2005; *Siddall et al.*, 2003], transitions from lowstand sea/lake to highstand sea/marine transitions are expected to occur at approximately 100 ka intervals in the Sea of Marmara [*Grall et al.*, 2012; *Sorlien et al.*, 2012; *Çağatay et al.*, 2009]. However, the depth of the Dardanelles sill varied with time as a consequence of erosion and sedimentation, probably in the 50–85 m range [*Çağatay et al.*, 2009] precluding a priori determinations of the precise timing of the transitions from global sea level curves.

[7] Environmental transitions, and associated variations in water level, also produced variations of sedimentation rates and stratigraphic sequence boundaries on the shelves, as well as in the basins [*Çağatay et al.*, 2003, 2009; *Seeber et al.*, 2006; *Sorlien et al.*, 2012; *Grall et al.*, 2012]. During the last lacustrine period, sedimentation rates in the basins may have been 2 or 3 times higher than during the marine period [*Çağatay et al.*, 2003; *Seeber et al.*, 2006; *Grall et al.*, 2012], and the frequency of submarine mass movements increased during the last marine ingression [*Zitter et al.*, 2012]. The topographic highs separating the basins are deeper than the shelves (300 and 600 m minimum depth). For this reason, they remained submerged during the last glacial cycle (and presumably throughout the Pleistocene) and followed the same general pattern of variation in sedimentation rate with time as the deep basins.

[8] A detailed record of sedimentation rates within lowstand sea/lake, highstand sea/marine sediments units, and during the last deglaciation period is provided by two long Marion Dufresnes cores (30m length, MD01-2430 and MD04-2741) [*Lericollais and Henry*, 2004, *Vidal et al.*, 2010] located on the Western High, south of the MMF, within the 3-D seismic survey. *Vidal et al.* [2010] provided a high-resolution age model of the core MD01-2430 over the last 23 ka, which we augmented by including the tephra layer found at 15 and 16.5 m depth in cores MD01-2430 and MD04-2741, respectively [*Lericollais and Henry*, 2004]. This tephra layer, 15 cm thick, is the Campanian Ignimbrite (Y-5) tephra dated (Ar/Ar age) at 39.3 ka B.P. [*De Vivo et al.*, 2001]). The age model shows that a sharp drop of sedimentation rate is associated with the deglaciation, as already observed in deep basins [e.g., *Seeber et al.*, 2006; *Beck et al.*, 2007; *Grall et al.*, 2012]. This period of low sedimentation rates (0.2 mm/a) lasted from 15,000 to 5000 years B.P. Sedimentation rate increased again over the last 5000 years from 0.2 to 0.4 mm/a [*Vidal et al.*, 2010], but not as much as glacial rates, which were about 0.5–0.6 mm/a. These variations could be explained by transient sediment storage on the shelf after sea level rise [*Zitter et al.*, 2012] and were, perhaps, facilitated by related variations in sediment transport dynamics and in the input from rivers and the Black Sea. In the deep basins, these variations of sedimentation rate are reflected in the geometry of deposits. For instance, echo sounder profiles show that the postglacial marine sediments display lateral variations in thickness and pinch out toward the edge of the basins, while the underlying lacustrine sediments do not [*Seeber et al.*, 2006; *Zitter et al.*, 2012]. In this work, we document stratigraphic sequences consisting of alternating draped and filling units, showing moderate and strong sediment thickness variations, respectively (Figure 3). Moreover, several of the filling units display onlap at their base. We hypothesize that these sequences correlate with glacial-interglacial cycles and that the filling units correspond to highstand deposits. In this case, episodes of slower sedimentation rate occurring at the end of each glacial periods would represent the sequence boundaries.

2.2. Stratigraphic Age Model Construction

[9] We calculate age estimates for the main reflectors from extrapolation of the average glacial/interglacial sedimentation rate, which is known locally from MD cores. This age model is then correlated with both the glacial/interglacial history and the age model of [*Sorlien et al.*, 2012] for the eastern Sea of Marmara. The age model is defined so that our sequence boundaries coincide with episodes of sea level rise.

[10] The sedimentation rates through the sedimentary sequences of the perched basins within the 3-D seismic survey were computed by downward extrapolation. The sedimentation rates were constrained by the depths of the uppermost horizon and dates from correlation with Marion Dufresnes cores [*Lericollais and Henry*, 2004]. The sedimentary records of the highs contain hiatuses, and thus, ages were extrapolated only within the perched basins, where sedimentation rates vary less within time. Ages were computed locally for each of the deeper horizons on a grid of regularly spaced points. We calculated the age for a given horizon by averaging the age computed over this grid, and estimated the probable age ranges, from the standard deviation of the age distribution obtained for each horizon. The standard deviation of the age distribution provides an estimate of the uncertainty resulting from progressive changes in basin geometry. A compaction model deduced from the velocity analysis of seismic reflection data was used for the sedimentation rate extrapolation. The *P* wave velocity with depth was determined by a linear regression ($V(z) = V_o + C \times Z$) [*Sheriff*, 1973; *Tolmachoff*, 1993], with V_0, the velocity at the seafloor in m/s, and C, the velocity gradient in s^{-1}. A relationship between porosity and depth is derived using a general relationship between *P* wave velocity and density for sediments given by *Brocher* [2005]. The porosity-depth relationship is approximated as an exponential (Athy's law), $\varphi(z) = \varphi_0$
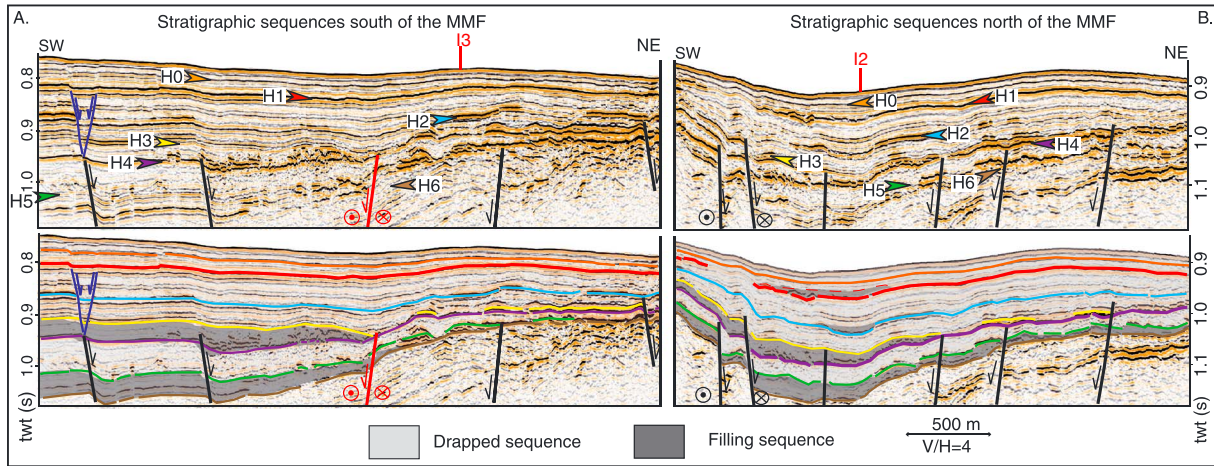
Figure 3. Comparison of stratigraphic sequences (a) south of the MMF and (b) north of the MMF with interpretations below (see locations in Figure 2b) along representative SW-NE seismic lines is shown. I2 and I3 are the intersections with the seismic lines represented on Figures 4 and 8, respectively. The vertical exaggeration is computed at 0.9 s TWT below the sea level for Figure 3a and around 1.0 s TWT below the sea level for Figure 3b. The main stratigraphic boundaries which can be recognized over most of the survey are indicated by solid lines, and the stratigraphic units are colored in light grey and dark grey. The repetition of four sequences which contains draped units (in light grey) with moderate lateral variations of thickness, and basin filling units (in dark grey) displaying strong lateral variations of thickness and laterally correlative with either condensed sections or erosions on the slopes and topographic highs, are recognized. Sedimentary bodies that contain irregular lenses and chaotic reflections are observed at the base and/or within the filling sequences and are interpreted as mass transport deposits (MTDs) (e.g., [*Alves*, 2010]).

exp $[-\alpha(z-z_0)])]$ where φ_0 is the porosity of the sediment on the seafloor, z_0 is the seafloor depth, and *a* is Athy's constant. The compaction model obtained was implemented in the downward extrapolation of sedimentation rates at the seafloor to estimate age ranges of the horizons. The age model represents the raw results of this extrapolation, and we show that it is compatible with an interpretation of stratigraphic sequences in terms of glacioeustatic cycles. The stratigraphic sequences recognized were correlated with the ones proposed by *Sorlien et al.* [2012], who correlated continuous reflectors in the eastern Sea of Marmara with lowstand wedges and deltas observed in the southern shelf of the Imrali Basin, interpreted as marking sea level minima. The constraints on this correlation are explained in more details in section 3.2.

3. Stratigraphic Model

3.1. Stratigraphic Sequences

[11] Stratigraphic sequences were primarily defined in perched basins and then laterally correlated. Several reflective horizons were traced, or correlated by comparison of reflective character and sequence, over most of the 3-D seismic volume. Correlation across the main fault was based on seismic facies analysis of the reflector sequences, which are nearly identical at locations with similar sedimentation rate (Figures 3 and 4).

[12] Starting from the seafloor, the first high-amplitude reflector is H1. It has a negative polarity, i.e., reversed from the polarity of the seabed (Figure 4). In ponded basin (Figure 4), H1 is contained within an onlap sequence. By this, we mean that several reflectors onlap on H1 but that the layer immediately below also pinches out toward the edges of the basin on a lower onlap surface (reflector H1′,

Figure 4), which coincides with H1 outside of the basin. Conversely, above and below the onlap sequence, reflectors are laterally continuous although some variations of layer thicknesses are observed. These characters suggest that H1 corresponds in the basins to a discrete sedimentary event, within an interval of sedimentation that is condensed on the topographic highs. At several locations, H1 displays erosional pinchouts and is overlain by chaotic bodies (Figure 4) interpreted as mass transport deposits (MTDs) [*Grall et al.*, 2014]. At greater depth, a layered unit (between H3 and H1, Figure 4), 40 to 110 m thick, can be recognized all over the 3-D data. Within this unit, a reflector (H2) displays characteristic lateral variations in amplitude and polarity (Figure 4). Within the ponded basins, onlapping reflectors, and rare chaotic reflections, are locally observed just above this horizon. Deeper, a prominent reflector with a positive polarity (H4) marks the top of a transparent layer (between H4 and H5); it shows a thickness of about 37 m in average and is observed all over the 3-D survey where signal penetration allows. The layers immediately above H4 displays large lateral variations in thickness (Figure 4) and even locally pinch out (Figure 4), with onlap geometry. Irregular lenses with chaotic reflections are also present above H4, as observed above H1 (Figure 4). Reflector H3, defined as the first regionally consistent reflector above H4, marks the transition between these laterally variable deposits, beneath, and draped sedimentary layers, above. Reflector H3 has small-scale topography that could correspond to small erosional gullies and/or sediment waves (Figure 4). Below the transparent layer, a new complex of sedimentary bodies is observed between reflectors H5 and H6. H5 has small-scale topography similar to H3, but often, topographies have higher amplitude on H5. H6 is found at the top of a transparent layer.
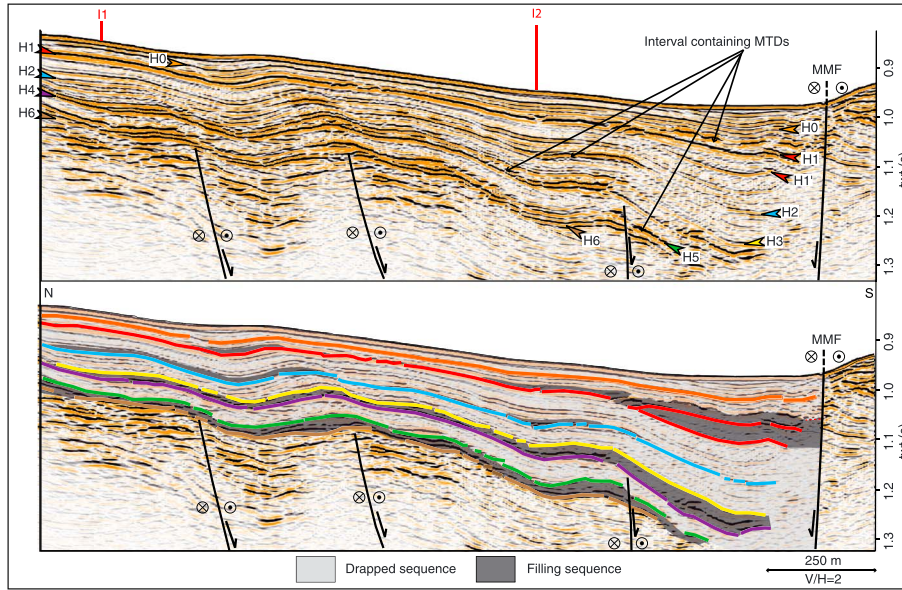
Figure 4. Representative N-S seismic section north of the MMF (see location in Figure 2b) with interpretation below is shown. I1 and I2 are the intersections with the seismic lines represented in Figures 8 and 5b, respectively. The vertical exaggeration is computed at 1.1 s TWT below the sea level. The colors and the horizon names are the same than on other seismic lines and on the age models (see Figures 4, 7, and 8). Horizon H1′ merges on H1, showing that this interval is condensed on topographic high. The fanning of sediment toward the MMF is well recognized for horizon above H2. For deeper horizons, the lateral variations of thickness within filling units are moderated, suggesting that the fanning toward the south is less developed during their deposits.

Deeper horizons are difficult to follow, mainly because of limited seismic penetration.

[13] In summary, we recognized four basin filling units on top of H1 and H2, between H3 and H4 and between H5 and H6. These basin filling units display strong lateral variations of thicknesses and laterally correlative with condensed sections (Figure 3) or erosion on the slopes and topographic highs and contains at the base and/or inside irregular lenses and chaotic reflections interpreted as mass transport deposits (MTDs) [e.g., *Alves*, 2010] (Figure 3). These basin filling units alternate with draped units which display moderate lateral variations of thickness, either acoustically transparent or bearing laterally continuous internal subparallel reflectors.

3.2. Horizon Age Assignment and Age Uncertainties

[14] The age model is based primarily upon the downward extrapolation of the sedimentation rates though the sedimentary column after correction for compaction. Sedimentation rates were derived from the first regionally defined seismic reflector beneath the seafloor, named H0, dated by correlation with cores [*Lericollais and Henry*, 2004] (Figures 2 and 6). At the coring site, H0 is found at the same depth (around 15 m, 19.5 ms two-way time (TWT) below seafloor (bsf)) as the tephra layer dated at ~39 ka. The mean sedimentation rates derived in this way represent an average over a highstand sea/marine period (between 0 and 14.5 ka) and a lowstand sea/lake period (between 14.5 to 39 ka). These sedimentation rates were used to construct the stratigraphic age model assuming that sediment input, although highly variable in the short term, remains steady at the first approximation, when averaged over glacial/interglacial periods of comparable duration, such as a 100 ka glacial cycle.

Downward extrapolation of sedimentation rates took into account the variation of P wave velocity with depth for TWT/depth conversion and for determining the effect of sediment compaction (porosity loss) during burial. Horizon time maps were converted to depth by using interval velocities obtained from velocity analyses along 2-D long-offset profiles (Figure 2 and Table 1). P wave velocity versus depth distribution is obtained with a linear regression in which the value of the velocity at the seafloor (V_0) is 1510 m/s and the value of the velocity gradient (C) is 0.88 s^{-1}, considering the sedimentary section from the seafloor down to H6 in the 3-D-box domain. We derived change of porosity with depth, according to Athy's law approximation, obtaining a value for the porosity of the sediment at the seafloor (φ_0) of 0.625 and an Athy's law constant (a) of 0.537 km^{-1}. This factor (a) is higher than those for the deep basins, where sedimentation rates are 3 to 10 times higher than on the topographic highs. For example, in the Tekirdag basin, the velocity gradient (C) is 0.6 s^{-1}, the porosity of the sediment at the seafloor (φ_0) is 0.625, and the Athy's constant (a) is 0.367 km^{-1}. These values are in good agreement with other velocity analyses [e.g., *Sorlien et al.*, 2012] and can be considered representative of compaction within the deep basins of the Sea of Marmara, where fluid escape from the clay-rich sediments is delayed in zones of high sedimentation because of their low permeability, resulting in a low compaction gradient. The age values and error estimates given in Table 1 were obtained by averaging calculated ages over the area of the basin domains and computing the standard deviation. The averaging area is the same for all reflectors except for H1′, which can only be identified in the depocenter of the eastern ponded basin. Hence, the average sedimentation rate calculated

Table 1. Data Set Used for Calculated Age Model[a]

Horizon	Interval* Velocities (m/s)	Mean Sedimentation Rate (mm/a)	Mean Sedimentary Thickness (m bsf) Compacted / Decompacted	Age (ka)
SF				
SF-H1*	*1510 ± 1*			
H1		0.4 ± 0.1	39 ± 8 / 39 ± 8	105 ± 13
H1'-H1*	*1510 ± 1*			
H1′		0.5 ± 0.1	74 ± 15 / 77 ± 16	141 ± 11
H2-H1′*	*1539 ± 10*			
H2		0.4 ± 0.05	86 ± 14 / 90 ± 16	245 ± 25
H3-H2*	*1594 ± 15*			
H3		0.4 ± 0.05	114 ± 6 / 120 ± 7	340 ± 24
H4-H3*	*1630 ± 20*			
H4		0.4 ± 0.05	152 ± 21 / 163 ± 23	448 ± 41
H5-H3*	*1660 ± 20*			
H5		0.4 ± 0.05	189 ± 16 / 204 ± 18	574 ± 46
H6-H5*	*1700 ± 20*			
H6		0.4 ± 0.05	220 ± 18 / 240 ± 21	661 ± 66
bsf (below seafloor)				

[a]Age model (Figure 5) is computed on grids (adjust for each horizon) of regularly spaced points (~1000 nodes) over the ponded basins where sedimentation rates are relatively high and do not appear to vary a lot in time. Horizon depths and sedimentary thicknesses are estimated by taking into account the *P* wave velocities by interval indicated in italics in the table. Velocities are computed within intervals indicated by asterisks in the first column of the table. Sedimentary thicknesses are decompacted by using an Athy's law. Horizon ages are computed and averaged by combining the sedimentation rates and the sedimentary thickness after decompaction over the grids.

from the depth of H0 is 0.4 mm/yr for all reflectors, except for H1′, for which it is higher in the zone where this reflector can be distinguished from H1.

[15] Stratigraphic boundary age estimates (Figure 5; ages are given by the Table 1) were interpreted in relation to the change in global sea level [*Siddall et al.*, 2003] and the marine isotope stages [*Lisiecki and Raymo*, 2005]. The stratigraphic boundaries appear to be well-correlated with episodes of rapid sea level rise/the ends of the glacial periods. H1′ would correspond to the beginning of marine oxygen isotope stage MIS-5 (130 ka), H1 to the end of MIS-5a (109 ka), and the condensed section between H1′ and H1 to the marine highstand MIS-5 (130–109 ka). This condensed section is thus interpreted as an analogue to the Holocene onlaps on the lacustrine-marine transition in the basins,

resulting from a temporary decrease of sedimentation rate [*Seeber et al.*, 2006; *Grall et al.*, 2014]. The sediments affected by the MTD observed above H1 were thus deposited during the later part of MIS-5 (under marine conditions [*Çağatay et al.*, 2009]) and likely destabilized after the disconnection of Sea of Marmara under brackish lake conditions [*Grall et al.*, 2014]. Conversely, H2 correlates with the MIS-8/MIS-7 transition and H3 with the MIS-10/MIS-9 transition. The uncertainty on the ages of deeper reflectors is larger. Nonetheless, the calculated ages suggest that H4 and H6 may correlate with lowstands MIS-12 (430 ka) and MIS-16 (640 ka), respectively. *Grall et al.* [2014] hypothesized that filling units (displaying important variations of thicknesses and containing MTDs) were analogous to those of the upper onlapping sequence, which includes horizons
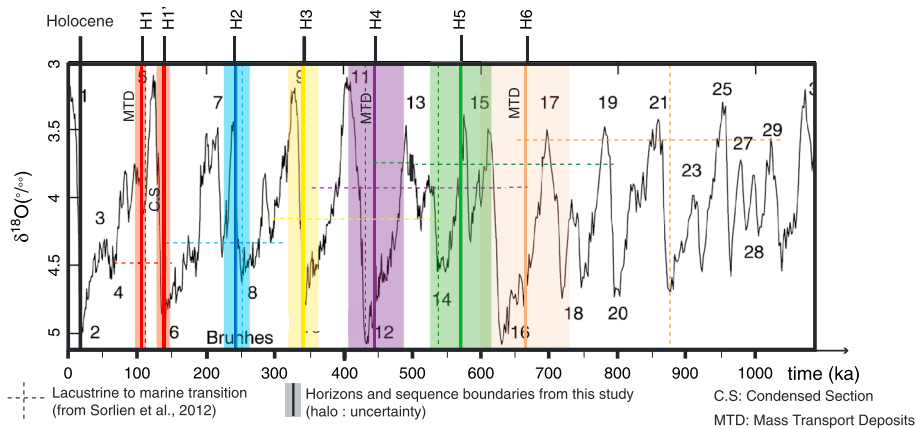

Figure 5. Computed ages of the stratigraphic sequence boundaries (red, H1; Blue, H2; Yellow, H3; violet, H4; green, H5; and brown, H6) are plotted on the global δO[18] curve (modified from *Lisiecki and Raymo* [2005]). The colors and the horizon names are the same than on seismic lines (see Figures 3, 4, 7, and 8) and in *Sorlien et al.* [2012]. The age model is obtained assuming a constant sedimentation rate through time. The solid lines and the haloes around correspond to the mean and the standard deviation of the age computed, respectively (refer to Figure 7 to see the zones where ages have been computed). The colors and the horizon names are the same than on seismic lines (Figures 3, 4, 7, and 8). The vertical dashed lines and the horizontal dashed lines represented the low sea/lake level to marine transition proposed by *Sorlien et al.* [2012].
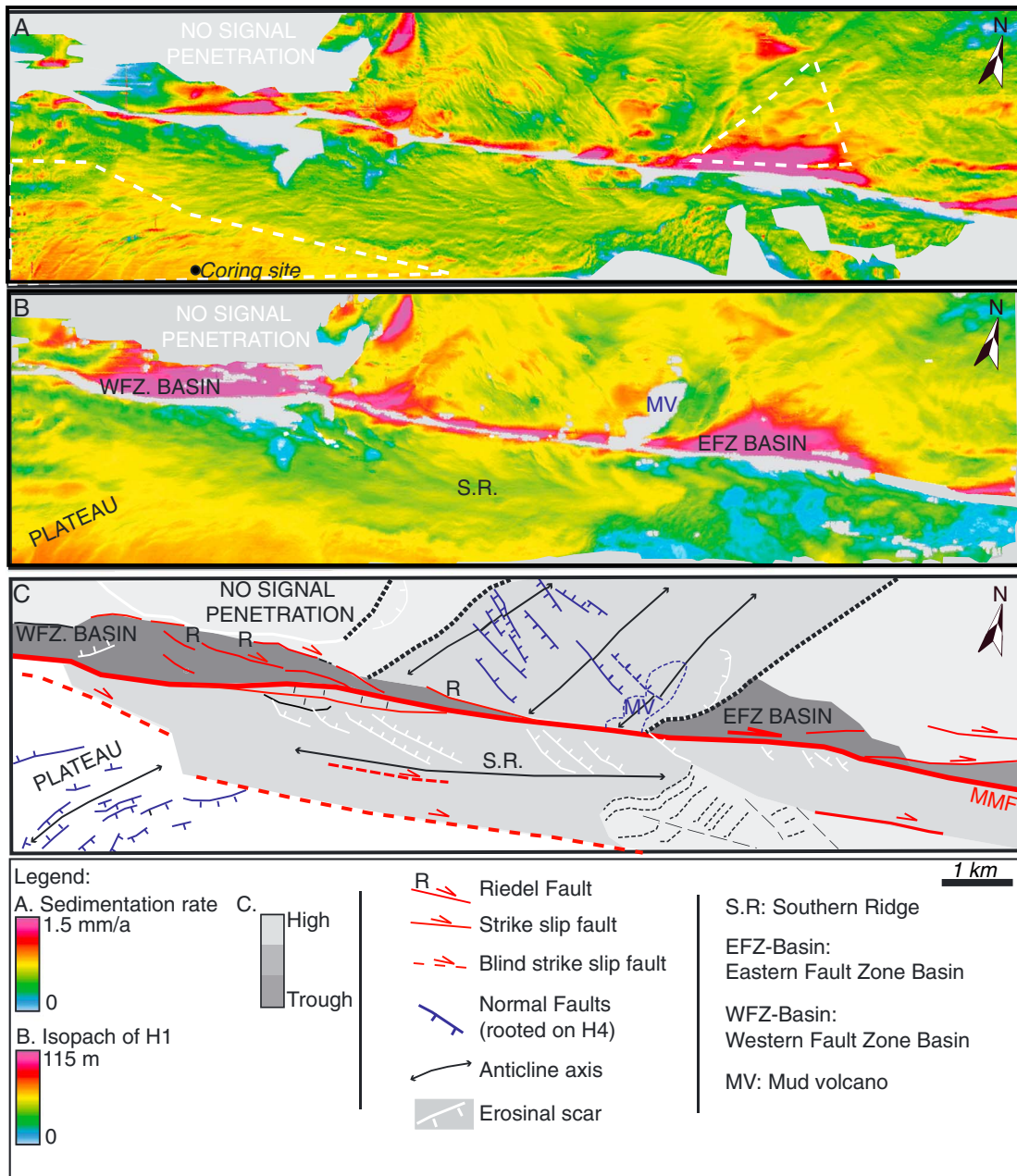
Figure 6. Morphological units, present-day sedimentation, and active main structures are shown. Mean sedimentation rate (for the last ~29 ka) over most of the 3-D survey derived from the H0-Seafloor isopach map and its probable age range according to core data. The dashed white lines located the zones where the age of horizons H1 to H6 have been computed, as no hiatus of sedimentation are observed in these areas. These areas have been gridded with around thousand dots (please refer to the text for more details about the calculations). H1-Seafloor isopach, representing the distribution of the sedimentation over probably the last 130 ka. Note the well fitted between this map and the map above, exceptions for the mud volcanoes which are buried by sediments above H1 and the erosive mass-wasting area in the eastern prolongation of the Southern Ridge, which appears currently more active. Synthesis of the main structures and the main morphological units over the last 130 ka. A strike-slip fault bounds the Southern Ridge and the Plateau, south of the MMF.

H1′ and H1 and MTDs. Age calculations suggest instead that the H4-H3 and H6-H5 intervals correspond to 100 kyr cycles, while the comparatively thinner filling sequences above H1′ and H2 correspond to shorter time intervals, correlative with highstands MIS-5 and MIS-7. The reason why two 100 ka sequences display larger lateral variations of sediment thickness than the others is still not understood. Stratigraphic sequences identified in the 3-D box were correlated with reflector sequences in the eastern Sea of Marmara, for which an age model has been proposed [*Sorlien et al.*, 2012]. This age model is based on the interpretation of deltas buried in the North Imrali Basin as lowstand markers and the
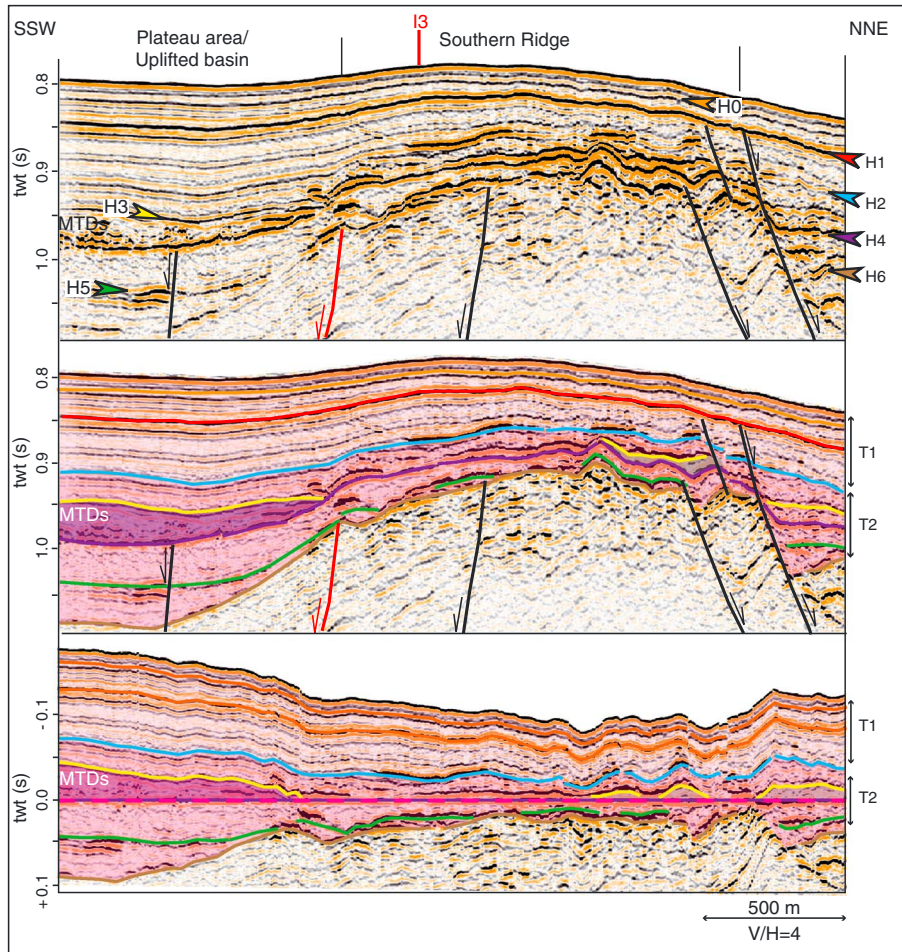
Figure 7. Representative WSW-ENE section north of the MMF (see location in Figure 2b) with interpretation below and flattened seismic section along the horizon violet (H4) is shown. I1 is the intersections with the seismic line represented in Figure 4. The vertical exaggeration is computed at 1.0 s TWT below the sea level. The colors and the horizon names are the same than on other seismic lines and on the age models (see Figures 3, 4, and 8). The blue faults correspond to fault maps on Figure 6, which mainly root on H4. The folding likely evolved through time, as the undulation of horizons above H2 (annotated period T1) is not in harmony with undulations of horizons below (period T2). The layer between H4 and H3 displays strong lateral variation of thickness and contains MTDs mainly on the eastern part. Horizon H3 pinches out eastward on H4 against the slope of a fold related to faults which display a normal component. These faults are mapped in Figure 10.

correlation of these deltas with seismic reflectors extending over the Central High, the Kumburgaz basin, and the SE Central Basin [*Sorlien et al.*, 2012]. Unfortunately, incision by canyons on the southern slopes of the Central Basin makes difficult correlations of reflectors shallower than H5 in the 3-D box with those in the eastern Sea of Marmara. The correlations we here propose are thus, in part, based on reflector character. Reflector H1 may be recognized over most of the Sea of Marmara as the first high-amplitude negative polarity reflector below the seafloor. Also, the acoustically transparent intervals between H4 and H5 and below H6 appear as characteristic features that can be recognized on both the Western High and the Central High. In addition, we proposed that onlap sequences in basins could be explained by rapid variations of sedimentation rates during and after episodes of rapid sea level rise. Consequently, they should correlate with the top successive lowstand deltas in

Imrali Basin. Integrating these constraints, we obtain the following correlation: H1-H1' correlated with Red-1, H2 with Blue-2, H4 with Purple-5, and H5 with Green-6; both stratigraphic age models, constructed with a similar approach, i.e., assuming that sediment input, although highly variable in the short term displays less variability when averaged over 100 ka glacial cycles, are consistent (Figure 5).

4. Structures and Possible Correlation of Sedimentary Bodies Across the MMF

[16] The MMF currently runs in a linear valley with an E-W orientation. Two small, narrow subsiding basins are observed along the north side of the MMF. These two fault-parallel troughs are hereafter called fault zone basins. The western fault zone basin opens westward to the deep Tekirdag basin, and the western part of the basin is collapsing above
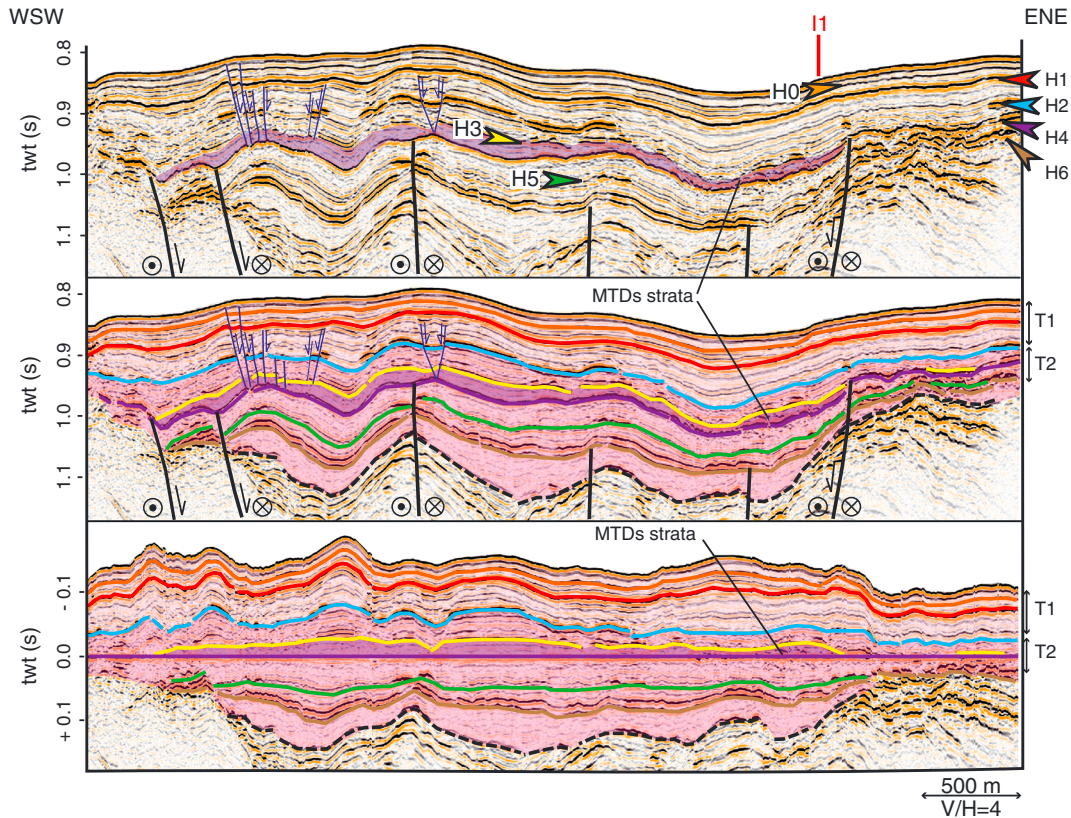
Figure 8. Representative SSW-NNE section south of the MMF (see location in Figure 2b) with interpretation below and flattened seismic section along the horizon violet (H4) is shown. I3 is the intersection with the seismic line shown in Figure 3. The vertical exaggeration is computed at 0.9 s TWT below the sea level. The colors and the horizon names are the same than on other seismic lines and on the age models (see Figures 3, 4, and 7). The topography of the plateau area (see Figure 6) evolved between the period 1 (above H2) and the period 2 (below H2). Thick chaotic intervals interpreted as MTDs occur within the H3-H4 layer as well as between the H5-H6 interval, and erosive channels are observed on the slope of the Southern Ridge, showing that this area collected MTDs from the ridge during the period 2 and has been then uplifted. Horizon H3 pinches out eastward on H4 against the faulting slope of the Southern Ridge. These faults are mapped in Figure 10.

listric faults. The basin is bounded to the north and south by two parallel faults. Vertical faults striking 15° clockwise of the bounding faults cross the basin (Figure 6) and are interpreted as Riedel R1 faults [*Riedel*, 1929; *Tchalenko and Ambraseys*, 1970]. The basin is thus interpreted as a narrow pull-apart basin between two parallel strands of the MMF, connected by Riedel shears (Figure 6). The sedimentation above H1 forms a fan thickening eastward, and in the eastern part of the basin, the imaging quality degrades beneath H1, displaying a reflective and chaotic acoustic basement. Layered sediments are imaged to deeper levels (>200 ms bsf) in the western part of the basin but can still not be regionally correlated below H1.

[17] The eastern fault zone basin displays a thick coherent sedimentary section with a maximum thickness of around 400 ms TWT along the MMF (Figure 4). The eastern fault zone basin is an asymmetric basin, in which sedimentary layers are progressively tilted toward the MMF; fanning is well developed between H2 and the seafloor, notably around H1 (Figure 4). Fanning on deeper horizons H4 and H6 is much less pronounced, indicating that most of the tilting toward the MMF occurred after the deposit of horizon H4.

[18] Between these basins, a 3 km wide mildly undulating topographic high roughly trend in the N045° direction (Figure 8). This high appears to be part of a larger scale in an en echelon N045° folding system (Figures 2 and 6). The geometry of the folds appears complex, probably because of a component of argillokinesis, as fluid-escape mounds are observed within the survey [*Tryon et al.*, 2012, 2010]. The folded layers are cut by escarpments-oriented N120° to N140° which correspond to normal faults. The N45° trending folds and small orthogonal normal faults indicate distributed deformation at shallow depth range (above H4, less than ~700 m depth below seafloor) within a right-lateral E-W strike-slip zone extending north of the fault at least over the width covered by the survey (1.5 km).

[19] South of the MMF, an elongated ridge, 2 km wide, hereafter called the Southern Ridge (Figures 6 and 7) runs parallel to the fault. The northern flank of this ridge displays N45° listric normal shear planes and tilted blocks (Figure 6), suggesting interaction between slope failure and strike-slip strain (Figure 6). These shear planes commonly cut the seafloor and H1 (Figure 6) and are regularly spaced, indicative of progressive creep-like deformation [*Shillington et al.*, 2012].

Slide scars also affect the eastern end of the ridge, where the orientation of slope failures appears primarily controlled by the slope toward the Central Basin. To the southwest, a gently sloping plateau extends in topographic continuity with the top of this ridge to the SW of the 3-D box (Figure 6). This plateau is a N225° broad anticline cut by faults parallel to its axis (Figures 6 and 4). These faults root at a shallow level (between H1 and H4). At a deeper level, blind faults with normal displacement affect H4 and layers below and strike about N120°, nearly orthogonal to the presently active ones, but consistent with the orientation of blind faults on the other side of the MMF (Figures 3 and 8). In the plateau area, basin filling sequences were deposited on H4 as well as H6 and display strong discontinuous reflections and incoherent intervals interpreted as MTDs (Figure 8). This indicates that what is now a topographic high area was previously a relatively low, collecting MTDs, and has then uplifted. The uplift of this area (hereafter called the uplifted basin) is one of several subtle but significant morphological changes that occurred between the deposition of horizon H4 and horizon H2.

[20] The stratigraphic sequences in this uplifted basin south of the main fault can be compared (Figure 3) in character, thickness, and geometry with the stratigraphic sequences observed north of the fault in an area extending from the topographic high to below the Eastern Basin. The basin filling layers H4-H3 and H6-H5 are found on both sides of the fault and thin toward the NE. Moreover, the MTD complex above reflector H4 is found on both sides, and its geometry and character suggest that it was a single continuous body extending across the present trace of the MMF (Figure 9). South of the fault, the top horizon of the layer containing MTDs above H4, horizon H3, pinches out against horizon H4 along a smooth onlap line trending N110°, following a buried fault scarp. The onlap line extends from the present-day main fault trace to the southern limit of the data set (Figure 9). At the level of H4, the Western flank of the Southern Ridge is disrupted by erosive mass wasting and is the probable main source of the slided material (Figure 8). North of the MMF, the interval between H4 and H3 also pinches out eastward, but the onlap line is jagged (Figure 9) with an average orientation N150°. Segments of the onlap line appear to follow N110°–N120° faults which present a normal component. This layer extends from the main fault zone to the northern limit of the data set and also contains lenses of incoherent reflections interpreted as MTDs (Figures 3 and 8). Most of the MTDs are observed within the eastern part of the layer, suggesting that the slided material also comes from the east (Figure 9b). Isopach maps bring further evidence of the geomorphology during the deposit of the MTDs. Lateral variations of thickness of the sequences are assumed to follow at least qualitatively the topography at the time of deposition. The isopach map of H4-H6 thus indicates that basins on both sides of the fault zone were bonded by ridges on their NE sides and that these ridges may have formed a continuous high; the general orientation of which was apparently controlled by N110°–N120° normal or transtensional faults (Figures 9 and 10). South of the fault, the N110° orientation of the buried ridge is distinct from the present orientation of the Southern Ridge. We return to this point below.

[21] The interpretation we propose implies a change in the strain distribution around the time of deposition of H4, the present regime probably being established around the time of deposition of H2 (Figures 6 and 10). One important point is to understand how the continuous ridge and basin system we propose could have been formed and subsequently cut by the MMF. It is possible that, at least in the shallow sediment, the slip was distributed between several fault strands, also with a larger component of diffused strain. In the present-day fault system, the Southern Ridge can be interpreted as a pressure ridge that formed along the transpressive segment of the MMF, located between the two fault zone basins. However, the NW-SE orientation of the buried ridge and basin system is not compatible with an origin as compressive system (Figures 9 and 10). One possibility to reconcile those interpretations is to consider that the growth of the Southern Ridge and the subsidence at its eastern end was determined by a curved strike-slip fault branch running along its southern edge and connecting westward to an array of N110–N120° normal or transtensional faults (Figures 9 and 10). This southern fault branch is recognized in the 3-D data set and still displays some local evidence of recent activity (Figure 6), but its kinematic importance is now small as most of the deformation now occurs north of the ridge, along the main fault trace and in a zone of distributed deformation further north. It is also possible that the bending of the ridge and basin system results at least in part from passive rotation within the strike-slip shear zone, especially considering the part of the ridge north of the MMF (Figures 9 and 10). One cannot elaborate further on the tectonic evolution of the North Anatolian Fault in the Western High solely on evidence from the 3-D data set, as it covers only a small area. However, the correlation of the stratigraphic sequences across the main fault appears to be a reliable result of the analysis of the 3-D data set that could not be achieved easily with 2-D seismic lines.

5. Mass Transport Deposits Correlation and Slip Rate Estimations

[22] Mass transport deposits immediately above H4 are found within the uplifted basin south of the MMF, as well as north of the fault. On both north eastern slopes of the basins (Figure 10), the sediments are disrupted by area of erosive mass wasting, which were presumably the source zones of the MTDs. The H4-H6 isopach map indicates that the unstable slope was dipping SW to SSW along the edge of N110°–N115° topographic high (Figure 9), bounded by faults with the same direction. Mass wasting observed on H4 suggests that sediment slid from the flanks of paleoridges, and large slides were deposited within basins, west of the ridges. It is unlikely that the similarity of the sedimentary deposits in the basins on both sides of the fault is a pure coincidence. The MTDs in both basins are probably part of the same complex, corresponding to the erosion products of a continuous ridge; these deposits appear to be right-laterally displaced by 7.7+/− 0.3 km along the MMF.

[23] All these observations lead us to propose that the MTDs in both basins are part of the same complex, corresponding to the erosion products of a N110° continuous ridge, and offset by the main strike-slip fault by 7.7 ± 0.3 km. It is, nonetheless, possible that the folds continued, at least for some time, to grow independently on either side of the fault and that the MTDs occurred at this time. It would result in overestimating the offset. It is, however, unlikely that the
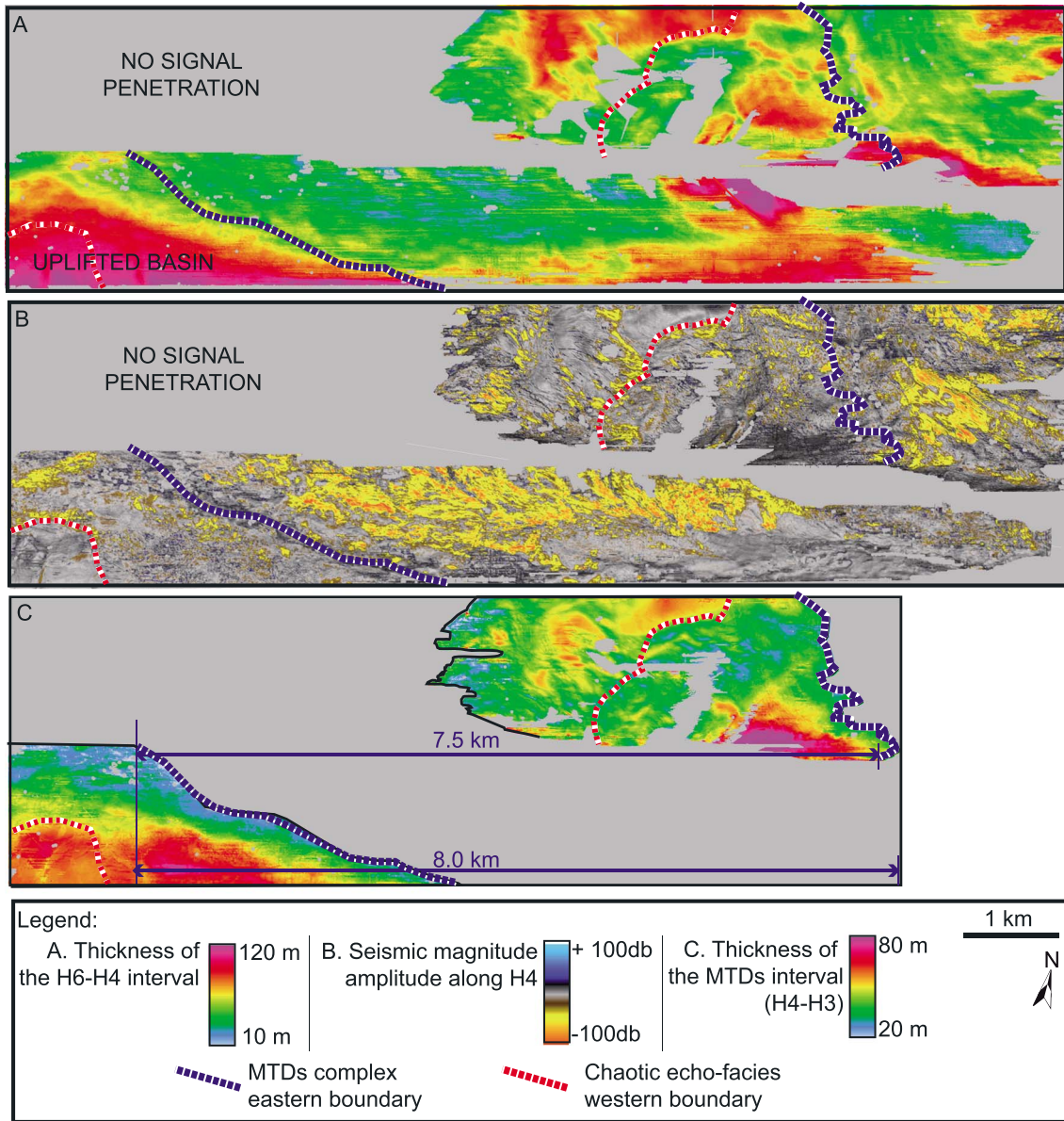
Figure 9. (a) H6-H4 isopach shows that the distribution of sedimentation over this possible glacial cycle does not match the present-day distribution (Figure 6). We assume that the distribution of sedimentation approximates the paleotopography during the deposit of the interval between horizons combined. South of the MMF, the MTDs layer follows precisely the faulting limit between the uplifted basin and the buried ridge. North of the MMF, the topography is more disturbed, but the MTDs layer ended on the flanks of topographic high which dips to the southwest. (b) Seismic amplitude magnitude along the horizon H4. Chaotic reflections at the base of the MTDs are recognized in the zone of slide depositions along the eastern boundary of the MTDs. Negative amplitude anomalies (refer to Figure 10) are trending in N110°–N120° strike and are associated to transtensive normal faults. (c) Isopach of the layer between H4 and H3 which contains MTDs, showing the possible offset of both sedimentary bodies.

similarity of the sedimentary deposits in the basins on both sides of the fault is a pure coincidence. Assuming a 7.7 ± 0.3 km displacement of the MTD starting from H4, the age model (H4 age = 405–490 ka, Figure 5 and Table 1) gives a slip rate of 15.1–19.7 mm/a.

[24] The accuracy of the estimated slip rate we obtain depends on the precise timing of the MTD and the MTD emplacement relative to the glacial cycles. We assigned it to the beginning of MIS-11 and thus to an episode of warming and global sea level rise, based on the following considerations. The base of this MTD complex lies on H4, which we correlated with the top of an unconformity at MIS-12 in the Imrali basin [*Sorlien et al.*, 2012], corresponding to a phase of sea level rise. A similar scenario of increasing mass-wasting event has been documented during the last deglaciation in the Sea of Marmara [*Görür and Çağatay*, 2010; *Ozeren et al.*, 2010; *Zitter et al.*, 2012], and the mass-wasting events cluster before the marine reconnection [*Beck et al.*, 2007;
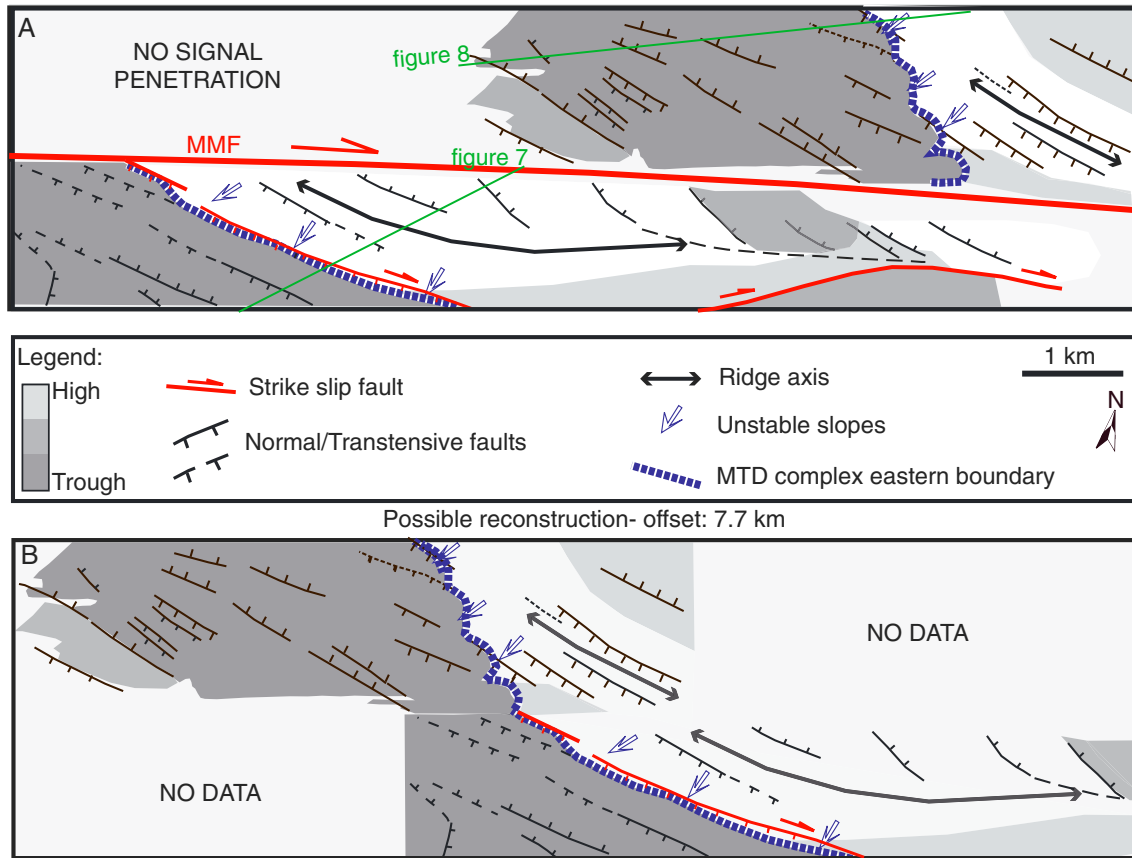
Figure 10. Morphostructural interpretation and mapping of the structures identified as active structures during the deposits of MTDs layer are shown. South of the MMF, the MTDs layer follows precisely the faulting limit between the uplifted basin and the buried ridge recognized on Figure 9. North of the MMF, the topography is more disturbed but the MTDs layer ended on the flanks of topographic high which dips to the southwest. The material forming the slide masses likely come on both sides of the fault from the northeast and glides along slopes faulting by N110°–N115° transtensive faults. There is possible reconstruction if we consider that the MTDs on both sides of the MMF are part of the same complex and have been then offset of 7.5–8 km by the MMF.

Ozeren et al., 2010; *Vidal et al.*, 2010]. The age proposed for Horizon H4 and the overlying MTD complex is consistent with the large-scale correlation of *Sorlien et al.* [2012], and the association of MTD occurrence with deglaciation, inferred for that episode, is also observed at the beginning of the Holocene in the Sea of Marmara.

6. Discussion and Conclusions

[25] Given the age constraints on the MTD complex cut by the MMF, which is displaced horizontally an estimated 7.4–8 km, the mean slip rate along the MMF since the deposition is 15.1 to 19.7 mm/a during the last 405–490 ka. This slip rate represents 75% of the total plate velocity between Anatolia and Eurasia [*Meade et al.*, 2002; *Le Pichon et al.*, 2003; *Reilinger et al.*, 2006; *Le Pichon and Kreemer*, 2010]. However, in evaluating this, shear partitioning between the northern and the southern branches of the NAF should be taken into account [*Flerit et al.*, 2003; *Reilinger et al.*, 2010; *Hergert and Heidbach*, 2010]. The present-day velocity across the Sea of Marmara is 18 ± 2 mm/a based on GPS [*Reilinger et al.*, 2010]. This value is compatible with the geological slip rate that we estimate for the MMF on the Western High if the MMF has been taking up nearly all of the strike-slip motion over the last 405,000–490,000 years. This would imply concentration of slip on a single fault on the Western High. As the strike slip in the eastern Sea of Marmara may be distributed between two or three fault splays [*Gasperini et al.*, 2011; *Bécel et al.*, 2010], it should merge to a single fault in the Western Sea of Marmara, perhaps, in part, along oblique structures such as the Imrali Fault (Figure 1b). Our slip estimate is not substantially different from that estimated for the single Ganos fault (18–24 mm/a), the westward continuation of the MMF on land [*Motagh et al.*, 2007]. In the 3-D data set, the MMF on the Western High appears as a boundary between a highly deforming domain to the north and a relatively less-deforming domain to the south of it which, at the large scale, may be considered as a flower structure [e.g., *Rangin et al.*, 2004]. However, unless the strike-slip rate of the Northern branch of the NAF has decreased over the last 405–490 ka, the fraction of plate motion accommodated by distributed deformation in the Western High or by secondary fault branches should be relatively small. Going further back in the past, we propose that a pressure ridge formed between 450 and 575 ka and was subsequently bent and crosscut by the present active MMF,

suggesting some changes in the distribution of deformation in this area. It is therefore possible that, in the past, deformation was more distributed over the Western High, but this does not necessarily imply a major change in kinematics in the Sea of Marmara. Changes in the strain distribution along this segment of the MMF might occur prior to 330, 000, as such changes which possibly resulted from local fault interaction [e.g., *Nicol et al.*, 2009] were also observed eastward within the Central Basin [*Grall et al.*, 2012].

[26] We conclude that strike-slip motion in the Western Sea of Marmara has been concentrated on the MMF over at least 450, 000 years and that, over this time interval, the MMF slipped at rates approximating to the total geodetic velocity across the Sea of Marmara. There are hints that the distribution of deformation has changed further back in the past, at least at the local scale of the 3-D high-resolution volume we interpreted, but this cannot be quantified from this data set alone. Mass-transport deposits across fault were used as an offset marker, and this approach could, perhaps, be applied to better constrain horizontal slip rates on faults at other locations in the Sea of Marmara and elsewhere.

References

Aksu, A., R. Hiscott, and D. Yasar (1999), Oscillating Quaternary water levels of the Marmara Sea and vigorous outflow into the Aegean Sea from the Marmara Sea Black Sea drainage corridor, *Mar. Geol.*, *153*, 275–302.

Alves, T. M. (2010), 3D Seismic examples of differential compaction in mass-transport deposits and their effect on post-failure strata, *Mar. Geol.*, *271*, 212–224, doi:10.1016/j.margeo.2010.02.014.

Armijo, R., B. Meyer, A. Hubert, and A. Barka (1999), Westward propagation of the North Anatolian fault into the northern Aegean: Timing and kinematics, *Geology*, *27*(3), 267–270.

Armijo, R., B. Meyer, S. Navarro, G. King, and A. Barka (2002), Asymmetric slip partitioning in the Sea of Marmara pull-apart: A clue to propagation processes of the North Anatolian Fault?, *Terra Nova*, *14*(2), 80–86.

Badertscher, S., D. Fleitmann, H. Cheng, R. L. Edwards, O. M. Göktürk, A. Zumbühl, M. Leuenberger, and O. Tüysüz (2011), Pleistocene water intrusions from the Mediterranean and Caspian seas into the Black Sea, *Nat. Geosci.*, *4*(4), 236–239.

Bécel, A., et al. (2009), Moho, crustal architecture and deep deformation under the North Marmara Trough, from the SEISMARMARA Leg 1 offshore-onshore reflection-refraction survey, *Tectonophysics*, *467*(1–4), 1–21.

Bécel, A., et al. (2010), North Marmara Trough architecture of basin infill, basement and faults, from PSDM reflection and OBS refraction seismics, *Tectonophysics*, *490*(1–2), 1–14.

Beck, C., et al. (2007), Late Quaternary co-seismic sedimentation in the Sea of Marmara's deep basins, *Sediment. Geol.*, *199*(1–2), 65–89.

Brocher, T. M. (2005), Empirical relations between elastic wavespeeds and density in the Earth's crust, *Bull. Seismol. Soc. Am.*, *95*(6), 2081–2092.

Çağatay, M. N., N. Gorur, O. Algan, C. Eastoe, A. Tchapalyga, D. Ongan, T. Kuhn, and I. Kuscu (2000), Late Glacial-Holocene palaeoceanography of the Sea of Marmara: Timing of connections with the Mediterranean and the Black Seas, *Mar. Geol.*, *167*(3–4), 191–206.

Çağatay, M. N., N. Görür, A. Polonia, E. Demirbag, M. Sakinc, M. H. Cormier, L. Capotondi, C. McHugh, O. Emre, and K. Eris (2003), Sea-level changes and depositional environments in the Izmit Gulf, eastern Marmara Sea, during the late glacial-Holocene period, *Mar. Geol.*, *202*(3–4), 159–173.

Çağatay, M. N., et al. (2009), Late Pleistocene-Holocene evolution of the northern shelf of the Sea of Marmara, *Mar. Geol.*, *265*(3–4), 87–100.

Carton, H., et al. (2007), Seismic imaging of the three-dimensional architecture of the Cinarcik Basin along the North Anatolian Fault, *J. Geophys. Res.*, *112*, B06101, doi:10.1029/2006JB004548.

De Vivo, B., G. Rolandi, P. B. Gans, A. Calvert, W. A. Bohrson, F. J. Spera, and H. E. Belkin (2001), New constraints on the pyroclastic eruptive history of the Campanian volcanic plain (Italy), *Mineral. Petrol.*, *73*, 47–65.

Flerit, F., R. Armijo, G. C. P. King, B. Meyer, and A. Barka (2003), Slip partitioning in the Sea of Marmara pull-apart determined from GPS velocity vectors, *Geophys. J. Int.*, *154*(1), 1–7.

Gasperini, L., A. Polonia, M. Namık Çağatay, G. Bortoluzzi, and V. Ferrante (2011), Geological slip rates along the North Anatolian Fault in the Marmara region, *Tectonics*, *30*, TC6001, doi:10.1029/2011TC002906.

Görür, N., and M. N. Çağatay (2010), Geohazards rooted from the northern margin of the Sea of Marmara since the late Pleistocene: A review of recent results, *Nat. Hazards*, *54*(2), 583–603.

Grall, C., P. Henry, D. Tezcan, B. M. de Lepinay, A. Bécel, L. Géli, J.-L. Rudkiewicz, T. Zitter, and F. Harmegnies (2012), Heat flow in the Sea of Marmara Central Basin: Possible implications for the tectonic evolution of the North Anatolian fault, *Geology*, *40*(1), 3–6.

Grall, C., P. Henry, G. K. Westbrook, M. N. Çağatay, Y. Thomas, B. Marsset, D. Borschneck, H. Saritas, G. Cifçi, and L. Géli (2014), Mass transport deposits periodicity related to glacial cycles and marine-lacustrine transitions on a ponded basin of the Sea of Marmara (Turkey) over the last 500 ka, in *Submarine Mass Movements and Their Consequences*, edited by S. Krastel et al., pp. 595–603, Springer International Publishing, Switzerland.

Hergert, T., and O. Heidbach (2010), Slip-rate variability and distributed deformation in the Marmara Sea fault system, *Nat. Geosci.*, *3*(2), 132–135.

Hubert-Ferrari, A., et al. (2002), Morphology, displacement, and slip rates along the North Anatolian Fault, Turkey, *J. Geophys. Res.*, *107*(B10), 2235, doi:10.1029/2001JB000393.

Imren, C., X. Le Pichon, C. Rangin, E. Demirbağ, B. Ecevitoğlu, and N. Görür (2001), The North Anatolian Fault within the Sea of Marmara: A new interpretation based on multi-channel seismic and multi-beam bathymetry data, *Earth Planet. Sci. Lett.*, *186*(2), 143–158.

Kaminski, M. A., A. Aksu, M. Box, R. N. Hiscott, S. Filipescu, and M. Al-Salameen (2002), Late Glacial to Holocene benthic foraminifera in the Marmara Sea: Implications for Black Sea-Mediterranean Sea connections following the last deglaciation, *Mar. Geol.*, *190*(1–2), 165–202.

Le Pichon, X., and C. Kreemer (2010), The Miocene-to-present kinematic evolution of the Eastern Mediterranean and Middle East and its implications for dynamics, *Annu. Rev. Earth Planet. Sci.*, *38*(1), 323–351.

Le Pichon, X., et al. (2001), The active Main Marmara Fault, *Earth Planet. Sci. Lett.*, *192*(4), 595–616.

Le Pichon, X., et al. (2003), The North Anatolian fault in the Sea of Marmara, *J. Geophys. Res.*, *108*(B4), 2179, doi:10.1029/2002JB001862.

Lericolais, G., and P. Henry (2004), Cruise report of Marmara VT/Marmacore 2, cruise IPEV VT68, http://p.f.henry.free.fr/marmara/index.html.

Lisiecki, L. E., and M. E. Raymo (2005), A Pliocene-Pleistocene stack of 57 globally distributed benthic d18O records, *Paleoceanography*, *20*, PA1003, doi:10.1029/2004PA001071.

Meade, B. J., B. H. Hager, S. C. McClusky, R. E. Reilinger, S. Ergintav, O. Lenk, A. Barka, and H. Ozener (2002), Estimates of seismic potential in the Marmara Sea region from block models of secular deformation constrained by global positioning system measurements, *Bull. Seismol. Soc. Am.*, *92*(1), 208–215.

Motagh, M., et al. (2007), Strain accumulation across the Gazikoy-Saros segment of the North Anatolian Fault inferred from Persistent Scatterer Interferometry and GPS measurements, *Earth Planet. Sci. Lett.*, *255*(3–4), 432–444.

Mudie, P. J., A. Rochon, A. E. Aksu, and H. Gillespie (2002), Dinoflagellate cysts, freshwater algae and fungal spores as salinity indicators in Late Quaternary cores from Marmara and Black seas, *Mar. Geol.*, *190*(1–2), 203–231.

Nicol, A., J. Walsh, V. Mouslopoulou, and P. Villamor (2009), Earthquake histories and Holocene acceleration of fault displacement rates, *Geology*, *37*(10), 911–914.

Oglesby, D. D., P. Martin Mai, K. Atakan, and S. Pucci (2008), Dynamic models of earthquakes on the North Anatolian fault zone under the Sea of Marmara: Effect of hypocenter location, *Geophys. Res. Lett.*, *35*, L18302, doi:10.1029/2008GL035037.

Okay, A. I., A. Kaşlılar-Özcan, C. İmren, A. Boztepe-Güney, E. Demirbağ, and İ. Kuşçu (2000), Active faults and evolving strike-slip basins in the Marmara Sea, northwest Turkey: A multichannel seismic reflection study, *Tectonophysics*, *321*(2), 189–218.

Okay, A. I., O. Tqysqz, and X. Kaya (2004), From transpression to transtension: Changes in morphology and structure around a bend on the North Anatolian Fault in the Marmara region, *Tectonophysics*, *391*(1–4), 259–282.

Ozeren, M. S., M. Namık Çağatay, N. Postacıoğlu, A. M. Celal Şengör, N. Görür, and K. Eriş (2010), Mathematical modelling of a potential tsunami associated with a late glacial submarine landslide in the Sea of Marmara, *Geo Mar. Lett.*, *30*(5), 523–539.

Parke, J. R., T. A. Minshull, G. Anderson, R. S. White, D. McKenzie, I. Kuşcu, J. M. Bull, N. Görür, and C. Şengör (1999), Active faults in the Sea of Marmara, western Turkey, imaged by seismic reflection profiles, *Terra Nova*, *11*(5), 223–227.

Parke, J. R., R. S. White, D. McKenzie, T. A. Minshull, J. M. Bull, I. Kuşcu, N. Görür, and C. Şengör (2002), Interaction between faulting and sedimentation in the Sea of Marmara, western Turkey, *J. Geophys. Res.*, *107*(B11), 2286, doi:10.1029/2001JB000450.

Parsons, T. (2004), Recalculated probability of M > = 7 earthquakes beneath the Sea of Marmara, Turkey, *J. Geophys. Res.*, *109*, B05304, doi:10.1029/2003JB002667.

Polonia, A., et al. (2004), Holocene slip rate of the North Anatolian Fault beneath the Sea of Marmara, *Earth Planet. Sci. Lett.*, *227*(3–4), 411–426.

Pondard, N., R. Armijo, G. C. P. King, B. Meyer, and F. Flerit (2007), Fault interactions in the Sea of Marmara pull-apart (North Anatolian Fault): Earthquake clustering and propagating earthquake sequences, *Geophys. J. Int.*, *171*(3), 1185–1197.

Rangin, C., et al. (2004), Strain localization in the Sea of Marmara: Propagation of the North Anatolian Fault in a now inactive pull-apart, *Tectonics*, *23*, TC2014, doi:10.1029/2002TC001437.

Reilinger, R., et al. (2006), GPS constraints on continental deformation in the Africa-Arabia-Eurasia continental collision zone and implications for the dynamics of plate interactions, *J. Geophys. Res.*, *111*, B05411, doi:10.1029/2005JB004051.

Reilinger, R., et al. (2010), Geodetic constraints on the tectonic evolution of the Aegean region and strain accumulation along the Hellenic subduction zone, *Tectonophysics*, *488*(1–4), 22–30.

Riedel, W. (1929), Zur mechanik geologischer brucherscheinungen, Zentralblatt fÅ¼r Mineralogie, *Geologie und PalÃ¤ontologie B*, *1929*, 354–368.

Ryan, W. B. F., C. O. Major, W. C. Pitman, K. S. Shimkus, V. Moscalenko, G. A. Jones, P. Dimitrov, M. Saking, and H. Y. Seyir (1997), An abrupt drowning of the Black Sea shelf, *Mar. Geol.*, *138*(1–2), 119–126.

Seeber, L., O. Emre, M.-H. Cormier, C. C. Sorlien, C. M. G. McHugh, A. Polonia, N. Ozer, and N. Cagatay (2004), Uplift and subsidence from oblique slip: The Ganos-Marmara bend of the North Anatolian Transform, Western Turkey, *Tectonophysics*, *391*(1–4), 239–258.

Seeber, L., M.-H. Cormier, C. McHugh, O. Emre, A. Polonia, and C. Sorlien (2006), Rapid subsidence and sedimentation from oblique slip near a bend on the North Anatolian transform fault in the Marmara Sea, Turkey, *Geology,* *34*(11), 933–936.

Sengor, A. M. C., et al. (2005), The North Anatolian Fault: A new look, *Annu. Rev. Earth Planet. Sci.*, *33*, 37–112.

Sheriff, R. E. (1973), *Encyclopedic Dictionary of Exploration Geophysics*, pp. 266, Society of Exploration, Geophysicists, Tulsa, Oklahoma.

Shillington, D. J., et al. (2012), Evidence for widespread creep on the flanks of the Sea of Marmara transform basin from marine geophysical data, *Geology*, *40*(5), 439–442.

Siddall, M., E. J. Rohling, A. Almogi-Labin, C. Hemleben, D. Meischner, I. Schmelzer, and D. A. Smeed (2003), Sea-level fluctuations during the last glacial cycle, *Nature*, *423*(6942), 853–858.

Sorlien, C. C., et al. (2012), Uniform basin growth over the last 500 ka, North Anatolian Fault, Marmara Sea, Turkey, *Tectonophysics*, *518–521*(0), 1–16.

Tchalenko, J. S. (1970), Similarities between shear zones of different magnitudes, *Geol. Soc. Am. Bull.*, *81*, pp. 1625–1640, doi:10.1130/00167606 (1970)81[1625:SBSZOD]2.0.CO;2.

Thomas, Y., B. Marsset, G. K. Westbrook, C. Grall, L. Géli, P. Henry, G. Çifçi, A. Rochat, and H. Saritas (2012), Contribution of high-resolution 3D seismic near-seafloor imaging to reservoir-scale studies: Application to the active North Anatolian Fault, Sea of Marmara, *Near Surf. Geophys.*, *10*(4), 291–301.

Tolmachoff, W. (1993), Linear velocity functions and the effect of mentors on the oil industry, Pac. Petr. Geol. Newsletter, Am. Assoc. Petr., Pacific Section (Geol).

Tryon, M. D., P. Henry, M. N. Çağatay, T. A. C. Zitter, L. Géli, L. Gasperini, P. Burnard, S. Bourlange, and C. Grall (2010), Pore fluid chemistry of the North Anatolian fault zone in the Sea of Marmara: A diversity of sources and processes, *Geochem. Geophys. Geosyst.*, *11*, Q0AD03, doi:10.1029/2010GC003177.

Tryon, M. D., P. Henry, and D. R. Hilton (2012), Quantifying submarine fluid seep activity along the North Anatolian Fault Zone in the Sea of Marmara, *Mar. Geol.*, *315–318*(0), 15–28.

Vidal, L., G. Ménot, C. Joly, H. Bruneton, F. Rostek, M. N. Çağatay, C. Major, and E. Bard (2010), Hydrology in the Sea of Marmara during the last 23 ka: Implications for timing of Black Sea connections and sapropel deposition, *Paleoceanography*, *25*, PA1205, doi:10.1029/2009PA001735.

Zitter, T. A. C., G. Celine, P. Henry, M. S. Ozeren, M. N. Cagatay, A. M. C. Sengor, L. Gasperini, M. Mercier De Lepinay, and L. Geli (2012), Distribution, morphology and triggers of submarine mass wasting in the Sea of Marmara, *Mar. Geol.*, *329–331*(0), 58–74.